Nuclear Physics A483 (1988) 371–405
North-Holland, Amsterdam

SYSTEMATICS OF COMPLEX FRAGMENT EMISSION IN NIOBIUM-INDUCED REACTIONS

R.J. CHARITY, M.A. McMAHAN, G.J. WOZNIAK, R.J. McDONALD and L.G. MORETTO

Nuclear Science Division, Lawrence Berkeley Laboratory, University of California, Berkeley, California 94720, USA

D.G. SARANTITES and L.G. SOBOTKA

Chemistry Department, Washington University, St. Louis, MO 63110, USA

G. GUARINO, A. PANTALEO and L. FIORE

Istituto Nazionale di Fisica Nucleare INFN, Sezione di Bari, Italy

A. GOBBI and K.D. HILDENBRAND

Gesellschaft für Schwerionenforschung, 6100 Darmstadt, West Germany

Received 12 January 1988

Abstract: Complex fragments of $3 < Z \lesssim 35$ have been detected in the reverse-kinematics reactions of ^{93}Nb plus ^{9}Be, ^{12}C and ^{27}Al at bombarding energies of $E/A = 11.4$, 14.7 and 18.0 MeV. Velocity spectra and angular distributions show the presence of projectile and target-like components along with a component isotropic (in the reaction plane). This latter component appears as a Coulomb ring in the invariant cross section plots indicating the presence of a binary decay which is confirmed by the coincidence data. Statistical model calculations indicate that for the Nb + Be and C reactions, the isotropic component is associated with the binary decay of compound nuclei formed in complete fusion reactions. The charge distributions for these two systems are consistent with the conditional barriers predicted with the rotating finite-range model. For the Nb + Al reactions, there is an additional isotropic component besides compound nucleus decay, which may arise from fast fission.

E NUCLEAR REACTIONS Be, C, Al(Nb, X), $E = 11.4$, 14.7, 18.0 MeV/nucleon; measured σ(fragment, E_X, θ), fragment-fragment coin. Statistical model calculations.

1. Introduction

At low bombarding energies (<10 MeV/nucleon), the formation of compound nuclei (CN) in fusion reactions and their sequential statistical decay have been extensively studied. Two commonly observed decay modes of the CN are the evaporation of light particles and fission. These modes are just two extremes of a more general binary decay mode [1]) involving the entire range of mass asymmetry.

0375-9474/88/$03.50

Compound nucleus decay has been shown to give rise to complex fragments, though at low bombarding energies such binary decays are exceedingly rare [2-4]) compared to neutron and light charged particle emission.

In general, the decay chain of a CN is associated with a number of sequential binary decays. The most common example of this is the formation of an evaporation residue by sequential emission of light particles. In the case of fission decay, the fission fragments themselves in turn may emit light fragments such as neutrons. Typically, in the latter case, the decay chain is associated with one near symmetric and a number of very asymmetric binary decays.

More recently, the concept of CN decay has been successfully applied to the intermediate energy regime (10-100 MeV/nucleon) [5-10]). CN produced in fusion reactions, and at the higher bombarding energies in incomplete fusion reactions, are formed with very large excitation energies and angular momenta. As a consequence, the intermediate asymmetry decay modes, which are rare at the low bombarding energies, become of increasing importance. Recent studies have found that CN decay is an important mechanism for the production of complex fragments at bombarding energies up to at least $E/A = 50$ MeV [refs. [8-10])]. These fragments were shown to be produced in a fission-like decay where only one binary division in the decay chain is not a light-particle evaporation. As the excitation energy of the CN increases, the decay chains become increasingly longer and more complex, and the production of three or more heavy fragments becomes possible.

For each possible binary division there is a conditional saddle-point configuration analogous to the ordinary saddle-point configuration in fission, except that the mass and charge asymmetries are constrained. The associated conditional barriers, together with the excitation energy, control the probabilities of the various decay modes. Some conditional barriers have recently been deduced from fitting complex fragment excitation functions [4]).

Experimental investigations of angular momentum dependent symmetric-fission barriers have been carried out by a number of groups [11-24]). Originally, experimental fission excitation functions were compared to statistical model calculations which employed rotating liquid-drop model (RLDM) [25]) fission barriers. Generally these studies concluded that the RLDM barriers needed to be reduced to fit the experimental data, though not all agreed with this conclusion [18]). Such a reduction in fission barriers agrees with the calculations of the rotating finite-range model (RFRM) [26]) which incorporates a Yukawa-plus-exponential form of the nuclear potential. These RFRM barriers have had moderate success in reproducing fission excitation functions obtained in heavy-ion induced reactions [20,21,23,24]). The finite-range model has also been successful in reproducing zero-angular momentum conditional barriers associated with the emission of complex fragments in ^{3}He induced reactions [27]).

Experimentally, the validity of the RFRM is best determined for light nuclei ($A \lesssim 100$) because for these the RFRM conditional barriers are 10 MeV or more lower than the corresponding RLDM barriers. Such light systems have a fissility

parameter below or near the Businaro-Gallone point [28]) and thus symmetric division is the least probable decay channel, except for very large angular momenta. The mass distributions of the decay products shows no significant fission peak. Measurements of the mass or charge distributions of complex fragments associated with all asymmetries provides a test of the statistical model and the RFRM conditional barriers. Whereas, in traditional fission studies one has to reproduce only the magnitude of the fission cross section, in complex fragment studies one needs to predict both the shape and magnitude of the charge or mass distribution.

Apart from the conditional barriers, there are other statistical model parameters needed to calculate the complex fragment distributions. As the values of many of these parameters are uncertain, and the predicted cross sections are sensitive to their exact values, it is not always clear to what extent RFRM conditional barriers are consistent or inconsistent with a measured mass or charge distribution. However, a systematic study of complex fragment emission would provide confidence in the validity of the statistical and rotating finite-range models if one could reproduce both the shapes and magnitudes of the mass or charge distributions over a large range of bombarding energies and of projectile-target combinations. Furthermore, systematic studies may allow one to establish the regions of excitation energy and angular momentum for which the standard statistical model calculations are valid and determine when effects such as nuclear dissipation [29-33]), temperature-dependent barriers [34-38]), fast-fission, or incomplete fusion are needed.

For these reasons, complex fragment emission from the reactions Nb + Be, C and Al at bombarding energies of $E/A = 11.4$, 14.7, and 18.0 MeV have been investigated. These experiments, in conjunction with previous studies of the same reactions at higher ($E/A = 25.4$ and 30.3 MeV) [8]) and lower ($E/A = 8.4$ MeV) [3]) bombarding energies, allow one to observe the evolution of complex fragment emission from the low to the intermediate energy regime. The use of reverse kinematics in this work was especially advantageous as it allowed one to detect and identify almost the entire mass range of complex fragments. Because of the large center-of-mass velocity in these reactions, even heavy fragments emitted with small velocities from the CN have a large laboratory velocity, thus allowing easy detection and identification.

The organization of the paper is as follows: The experimental details are given in sect. 2. In sect. 3, the results of the experiment are presented and the separation of complex fragments of CN origin from the target-like and projectile-like components is discussed. The experimental charge distributions are compared to statistical model calculations in sect. 4. Finally, the conclusions of this work are presented in sect. 5.

2. Experimental method

The experiment was performed at the Unilac of the Gesellschaft für Schwerionenforschung in Darmstadt. Beams of ^{93}Nb projectiles with energies of 11.4, 14.7, and

18.0 MeV/nucleon impinged on targets of ^{9}Be (1.6 mg/cm^2), ^{12}C (0.4 mg/cm^2), and ^{27}Al (1.4 mg/cm^2).

The main experimental techniques have been described previously [8]) and will be discussed here only briefly. Particles were detected in two position-sensitive, E-ΔE telescopes. The energy loss of a particle entering the telescope was measured with a gas ionization chamber operated with 60 Torr of CF_4 gas and the residual energy was measured with a 2 mm thick, Li-drifted Si detector. Both telescopes were positioned symmetrically on either side of the beam axis at angles from 8° to 20° and had acceptance angles of 8.4°.

The energy and position calibrations of the E and ΔE detectors were performed using the methods described in ref. [8]), with elastically scattered Nb projectiles from a 0.5 mg/cm^2 Au target and alpha particles emitted from a ^{212}Pb source. The energy calibrations were accurate to ±2% and the position resolution obtained was ±0.2°.

The atomic charge of the detected particles was determined from the measurements of E and ΔE. A typical example of a Z spectrum is shown in fig. 1, where peaks associated with particles of atomic number up to $Z = 36$ are clearly observed.

Absolute cross sections were determined from the beam charge collected in a Faraday cup. Inclusive and coincidence events between the two telescopes were recorded on magnetic tape and analyzed off-line.

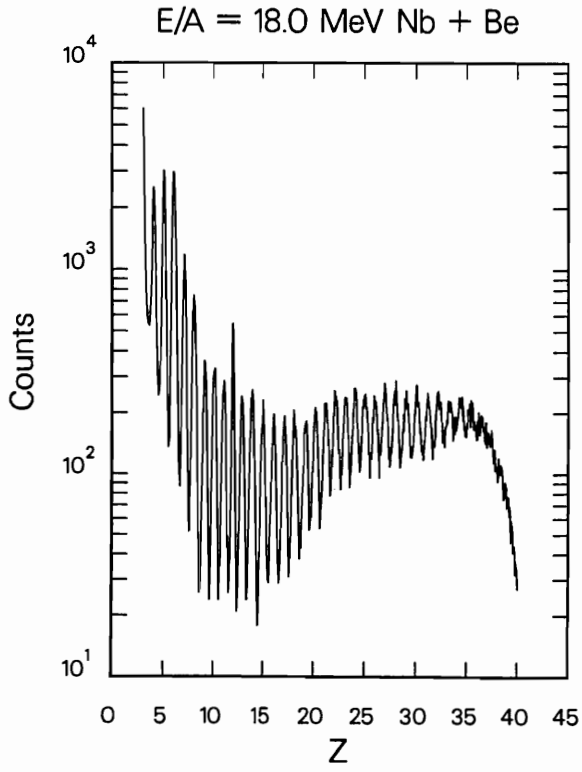

Fig. 1. Histogram showing the charge resolution obtained in this work.

3. Results

3.1. VELOCITY DIAGRAMS

Velocity spectra were obtained for each complex fragment Z-species. The velocity of a fragment was determined from its measured energy assuming an atomic mass number given by [8])

$$A = 2.08\,Z + 0.0029\,Z^2\,, \tag{1}$$

where Z is the measured atomic number of the fragment. This parameterization was obtained from a simulation of the decay of highly excited primary fragments by light-particle evaporation. It gives the predicted average atomic number of secondary fragments as a function of their Z-value and is valid only when the initial excitation energy of the primary fragments is greater than 1 MeV/nucleon. Over the range of fragments $5 \leqslant Z \leqslant 40$, it is estimated to be accurate to within ± 0.5.

Figs. 2 and 3 show linear contour plots of the cross section $(\partial^2\sigma/\partial V_{\parallel}\,\partial V_{\perp})$ in the $V_{\parallel} - V_{\perp}$ plane for representative Z-species detected in the Nb + Be and Al reactions at $E/A = 18.0$ MeV. The dashed lines indicate the maximum and minimum angles covered by the detectors and their low-velocity threshold. The large angular coverage obtained for the Nb + Al reaction in fig. 3 was derived from three angular positions of the detectors, whereas for the Nb + Be reaction in fig. 2 the angular coverage was obtained with only one position. These plots show for all the fragment Z-values the presence of an isotropic component $(\mathrm{d}\sigma/\mathrm{d}\theta = \text{const.})$ associated with the binary decay of systems produced in a fusion-like reactions. For some Z-values one can also see target-like and projectile-like components.

The compound binary-decay component is characterized by the uniform Coulomb rings, portions of which are seen for all Z-values in figs 2 and 3. The velocity associated with the center of the rings corresponds to the velocity of the source from which the fragments are emitted, and their radius corresponds to the velocity with which the fragments were emitted by the source. The emission velocity of each fragment is determined mainly by the Coulomb repulsion between the fragment and its partner and is approximately given by:

$$V_e = \sqrt{\frac{2M_2E_{\mathrm{Coul}}}{(M_1+M_2)M_1}}\,, \tag{2}$$

where M_1 and M_2 are the masses of the fragment and its partner, respectively, and E_{Coul} is the Coulomb energy between the fragment at scission. Since $E_{\mathrm{Coul}} \propto Z_1Z_2$ and assuming $Z \tilde{\propto} M$, then

$$V_e \tilde{\propto} Z_s - Z_1\,, \tag{3}$$

where $Z_s = Z_1 + Z_2$ is the atomic charge of the source system which underwent binary decay. The decreasing emission velocity with increasing fragment Z-value is reflected in the smaller Coulomb rings for the larger Z-values in figs. 2 and 3. The widths of the rings result from fluctuations in the Coulomb energy, sequential evaporation of light particles from the primary fragments, fluctuations in the source velocity, and the presence of different isotopes for a given Z-value.

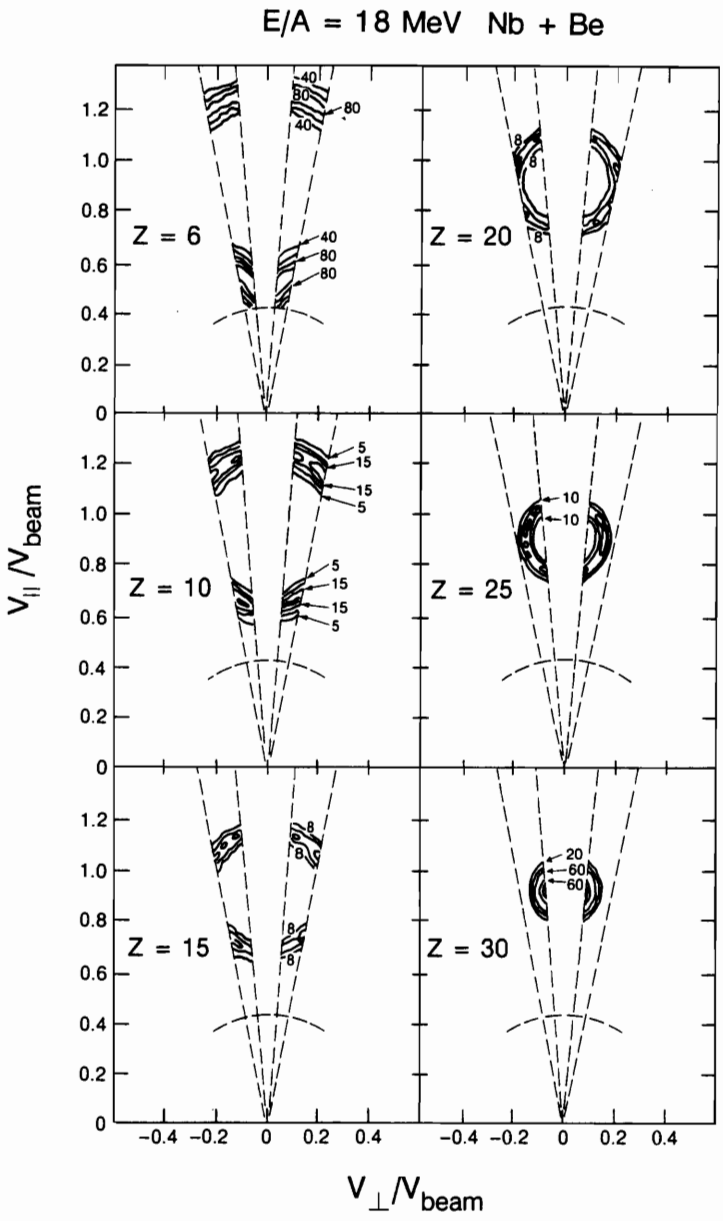

Fig. 2. Contours of the experimental cross section $\partial^2\sigma/\partial V_{\parallel}\,\partial V_{\perp}$ in the $V_{\parallel} - V_{\perp}$ plane for representative fragment Z-values detected in the reaction $E/A = 18.0$ MeV Nb + Be. The beam direction is vertical. The dashed lines show the maximum and minimum angular thresholds and the low-velocity threshold of the detectors. The magnitudes of the contour levels indicated are relative.

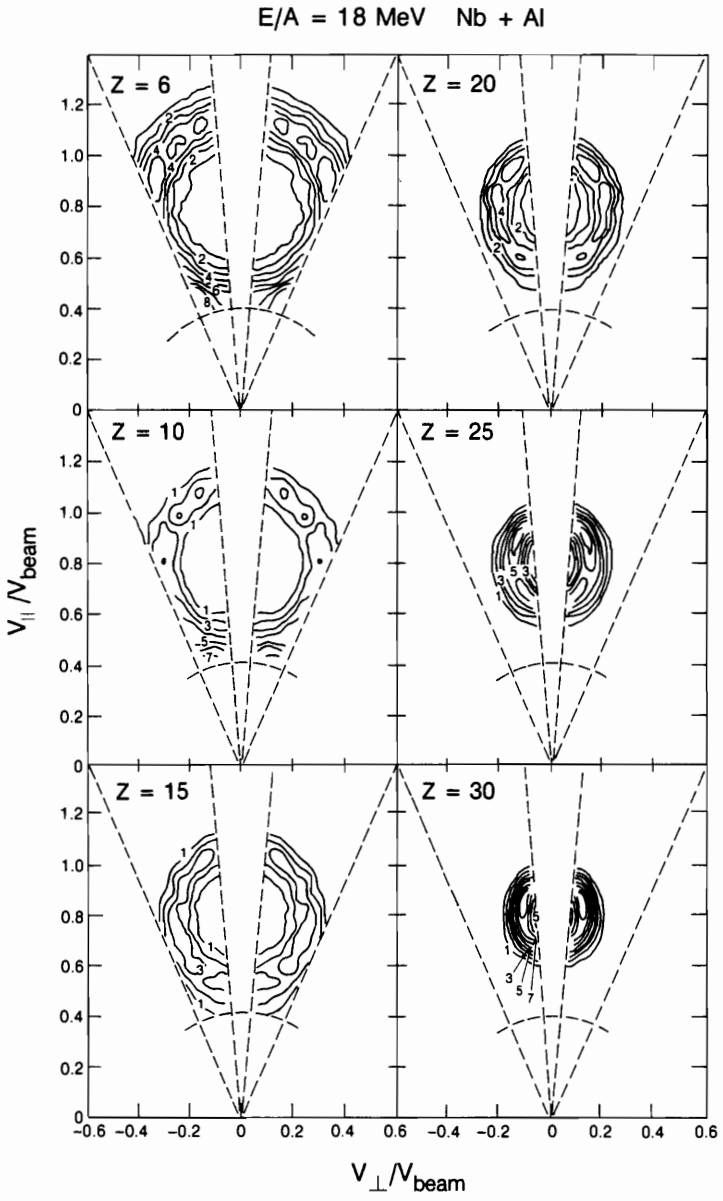

Fig. 3. Same as in fig. 2, for the reaction $E/A = 18.0$ MeV Nb + Al.

Target-like and projectile-like components are also observed in figs. 2 and 3. The target-like component (visible for $Z < 10$ for the Nb + Be reaction and $Z < 15$ for the Nb + Al reaction) corresponds to an additional yield in the backward direction. For the Nb + Al reaction, a projectile-like component is also observed. It is associated with the increased yield in the forward direction for fragments of $Z > 27$. For the

Nb + Be reaction, the projectile-like component is not observed, though it is presumably present at larger Z-values. For the lower bombarding energies, the target-like component, if still present, was not detected as it fell below the low-velocity threshold of the detectors. However, the projectile-like component was seen in the Nb + Al reactions at all the bombarding energies studied.

The origin of the target-like component is not completely clear, though it has been observed in a number of heavy-ion induced reactions [8,10,39,40]) and in some ^{3}He induced reactions [41,42]). (Projectile-like fragments in normal kinematics are target-like fragments in the equivalent reverse-kinematics reaction.) This component is associated with momentum transfers equal or lower than those of the isotropic component and thus can probably be interpreted as quasi-elastic or deep inelastic processes from more peripheral collisions [40,42]). The projectile-like component is presumably the complement of the target-like component. These two components need to be subtracted from the isotropic component when comparing with statistical model calculations.

3.2. SOURCE VELOCITIES

The source velocities give an indication of the degree of fusion associated with the reactions producing complex fragments. The source velocity is smallest for complete fusion and becomes larger as fewer of the target nucleons fuse with the projectile.

The source velocity was extracted from the Coulomb rings for each Z-species. The center of each ring was obtained from the following procedure: A test center was first chosen. In the frame associated with this test center, the velocity (V_e) and theta angle (θ_e) of each detected particle were calculated. The mean velocities associated with a number of different angular bins were then determined. These mean velocities were fitted to the polar equation for a circle whose center is offset from the origin. The offset obtained from this fitting procedure was added to the velocity of the test center to give the experimental source velocity. For the lower Z-values where the target-like component was present, a source velocity was obtained by using the leading edge of the velocity spectrum instead of its mean. The extracted ratios of source velocity relative to beam velocity (V_{source}/V_{beam}) are plotted as a function of Z-value in fig. 4. No source velocities were obtained for low Z-values at the lower bombarding energies as the fragments emitted at backward angles were below the low velocity threshold. For the reaction Nb + Be at $E/A = 11.4$ MeV, four consecutive Z-values were binned together in order to obtain sufficient statistics to extract the source velocity. The error bars plotted on each data point in fig. 4 represent the statistical error associated with the extraction process. The single large error bar for each data set indicates an estimate of the systematic error due to the energy calibrations and the mass parameterization.

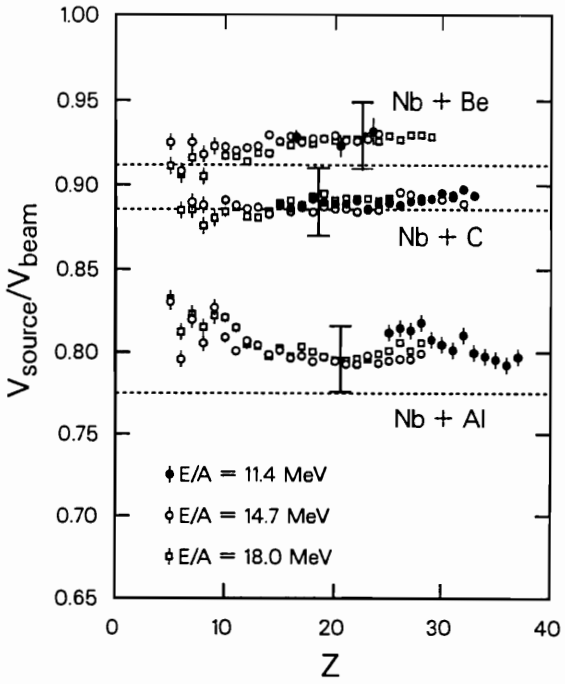

Fig. 4. Source velocities extracted from the Coulomb ring for each Z-species. The small error bar on each point indicates the statistical error associated with the extraction process. The single large error bar for each data set indicates the possible systematic error. Note the suppressed zero on the ordinate.

The dashed lines in fig. 4 represent the source velocity one would expect for a complete fusion reaction. For an incomplete fusion reaction, the source velocity is larger than this value. The experimental source velocities correspond to a high degree of fusion and are all consistent with complete fusion. It is interesting to note that the source velocities show no dependence on the bombarding energy. If the CN are being produced in incomplete fusion reactions, one would expect that the degree of incomplete fusion (and thus V_s/V_b) should increase as the bombarding energy increases. As this is not observed, it appears that the isotropic component is associated with complete fusion. Therefore the observed discrepancies of the data with the dashed lines (complete fusion) in fig. 4 are to be attributed to a systematic error.

In incomplete fusion reactions there is a reduction in the angular momentum and excitation energy transferred to the CN. This results in an initial sizeable reduction [8]) in the probability of complex fragment emission. Thus, if both complete and incomplete fusion processes are present in these reactions, as is suggested by the systematics [43]) of momentum transfer, the complex fragments may be associated predominantly with the former [8]).

The experimental source velocities show a small dependence on the fragment Z-value. This may be due to the inadequacies of the mass parameterization of eq. (1). Also, for Z-values where either the target-like or projectile-like components are present, the inability to separate these components completely from the fusion-like components may have led to errors in extracting the source velocity. One should also note, that at higher bombarding energies, Auger *et al.*[9]) have observed a dependence of the source velocity on fragment mass which they explain in terms of incomplete fusion.

3.3. EMISSION VELOCITIES

Figs. 5 and 6 show some examples of fragment velocity spectra in the source frame. For a number of representative Z-values, velocity spectra for both a backward

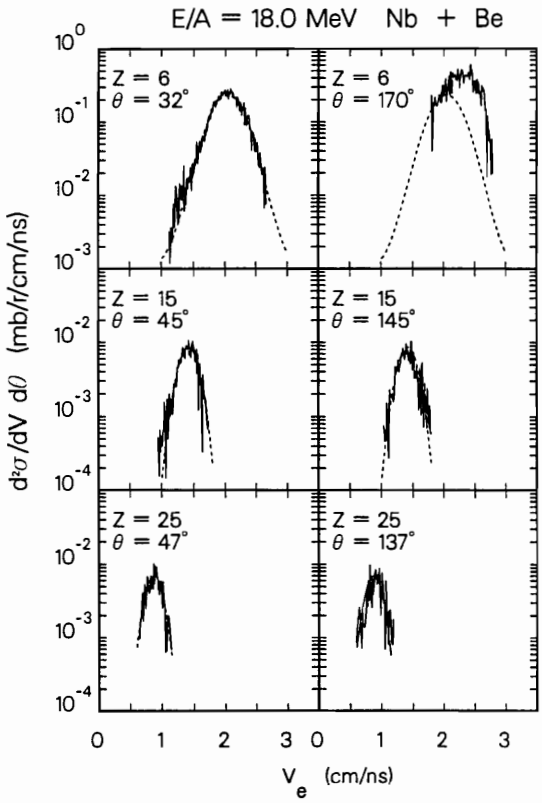

Fig. 5. Representative emission-velocity spectra of fragments in the frame of the source system for the reaction $E/A = 18.0$ MeV Nb+Be. For each Z-species, forward and backward angle spectra are shown. The dashed curve is a fit to the forward angle spectrum. It is also plotted with the backward-angle spectrum for comparison.

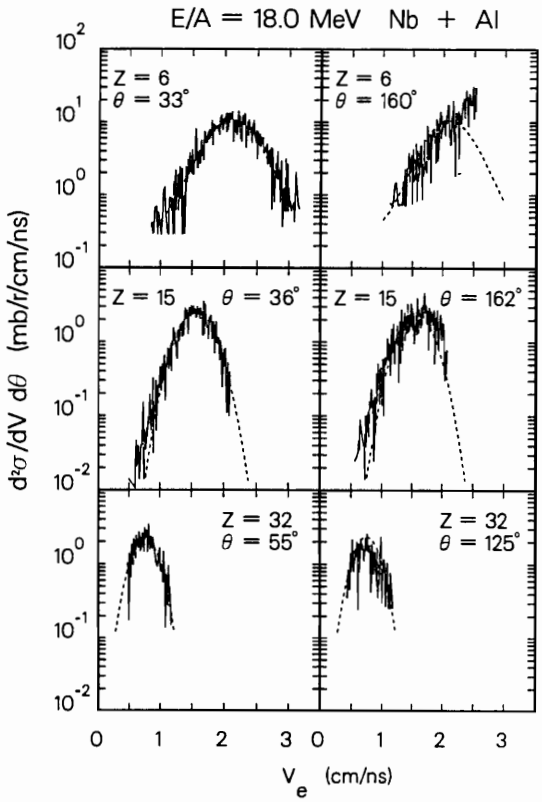

Fig. 6. Same as in fig. 5, for the reaction $E/A = 18.0$ MeV Nb + Al.

emission angle and a forward emission angle are shown. The dashed curves are fits to the forward angle spectra. These same curves are plotted with the backward angle data for comparison. For the larger Z-values, where only the isotropic component is present, the forward angle and backward angle spectra are very similar in both shape and magnitude with the shape being approximately gaussian. For fragments of $Z = 6$, one notices that the backward angle spectra peak at larger velocities and have larger yields than the forward angle spectra. This is, of course, due to the presence of the target-like component at the backward angles.

The first and second moments of the velocity spectra associated with the isotropic component are plotted versus Z-values in fig. 7. For Z-values where the target-like or projectile-like components are present, these moments were obtained only from the backward angle or forward angle spectra, respectively.

The approximately linear decrease of the emission velocity with fragment Z-value predicted by eq. (2) is clearly seen in fig. 7. The emission velocities show only a small dependence on the bombarding energy. The biggest effect is seen for reactions with the Al target, where the emission velocities decrease by 6% to 8% as the

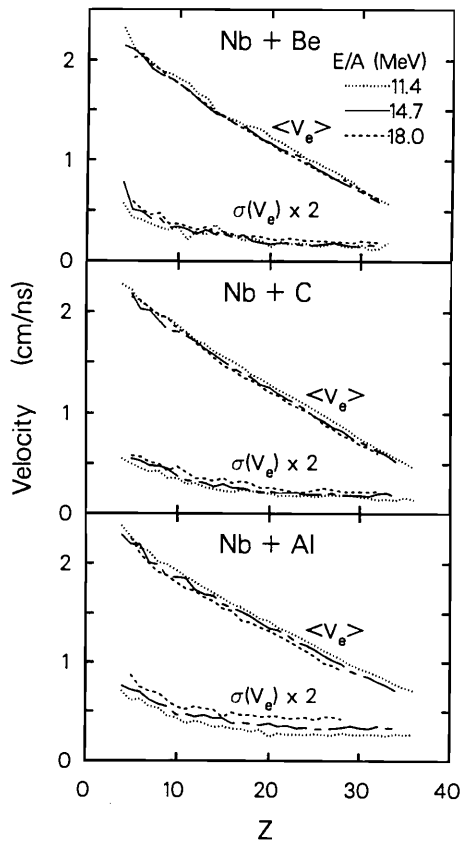

Fig. 7. First and second moments of the velocity spectra for each Z-species. To show the three bombarding energies on the same plot, lines are used rather than the data points.

bombarding energy increases from $E/A = 11.4$ MeV to $E/A = 18.0$ MeV. One should remember that we are seeing the decrease of emission velocities associated with a particular secondary Z-value, that is the Z-value of the primary fragment after the sequential evaporation of light particles. It would be more illuminating to observe the dependence of the emission velocities with the primary Z-value. Table 1 lists the secondary Z-values associated with symmetric division (Z_{sym}). These were obtained from the coincidence data (see sect. 3.6). As the bombarding energy increases this Z-value decreases. The corresponding emission velocities interpolated from fig. 7 for symmetric division are also listed. Higher bombarding energy data from ref. [8]) have also been included. These emission velocities show no dependence on the bombarding energy and are equal within the experimental error.

From the emission velocities, the kinetic energy release for symmetric division was calculated assuming a source system of atomic number $Z_p + Z_t$. If the atomic number of the fissioning system is smaller than this, it will result in an overestimation of the kinetic energy release. The experimental kinetic energy releases are compared

TABLE 1

The experimental emission velocities associated with symmetric division. The secondary Z-value corresponding to symmetric division is also listed

Target	E/A (MeV)	Z_{sym}	V_e (cm/ns)
Al	11.4	24.1	1.21 ± 0.03
	14.7	23.1	1.20 ± 0.03
	18.0	22.2	1.21 ± 0.03
	25.4	19.9	1.18 ± 0.05
	30.3	19.2	1.19 ± 0.05
C	11.4	22.9	1.11 ± 0.03
	14.7	22.5	1.17 ± 0.03
	18.0	21.8	1.14 ± 0.03
Be	11.4	22.1	1.24 ± 0.03
	14.7	22.0	1.08 ± 0.03
	18.0	21.6	1.12 ± 0.03
	25.4	20.9	1.06 ± 0.05
	30.3	20.2	1.11 ± 0.05

The errors listed are the statistical errors associated with extracting the emission velocity from the data.

to the values obtained from the systematics of Viola [44]) in table 2. The experimental values are consistently larger than the Viola systematics. However, in the Viola systematics, the kinetic energy released is an average over a range of mass and charge divisions. For light systems, this range can be quite large, and as the kinetic energy release is largest for symmetry division, the average is weighted towards smaller values. This may explain the observed difference between the Viola systematics and our experimental data.

TABLE 2

Experimental kinetic energy released in symmetric binary division compared with the predictions of the empirical formula of Viola [44])

Target	E_{kin} (exp) (MeV)	E_{kin} (Viola) (MeV)
Be	70 ± 8	59 ± 2
C	69 ± 3	63 ± 2
Al	91 ± 4	78 ± 2

The experimental error is the systematic error which is larger than the statistical error.

3.4. ANGULAR DISTRIBUTIONS

The experimental angular distributions of complex fragments are very useful for differentiating the contributions from the various components. The $d\sigma/d\theta$ distributions in the frame of the source system were determined for all fragment Z-values. Figs. 8–10 show some representative examples of these. For the $E/A = 18.0$ MeV Nb + Al reaction (fig. 9), one can clearly see the presence of the three components. At intermediate Z-values, the distributions are flat, indicating that these fragments were emitted isotropically in the reaction plane. In addition, for all Z-values, there is an isotropic region. For fragments with $Z \leq 18$, the distributions are peaked at backward angles due to the presence of an additional target-like component. The projectile-like component is associated with the forward peaking of the distributions for $Z \geq 28$. These features have been observed previously in normal kinematics reactions and have been interpreted as due to quasi-elastic and deep inelastic processes. For example, the very similar systems (^{14}N and ^{20}Ne + ^{107,109}Ag) have been extensively studied at bombarding energies below 12.5 MeV/nucleon [45,46]).

For the $E/A = 18.0$ MeV Nb + Be reaction (fig. 8), the backward peaking of the distributions is again visible for light fragments ($Z < 10$). Unfortunately, the distribu-

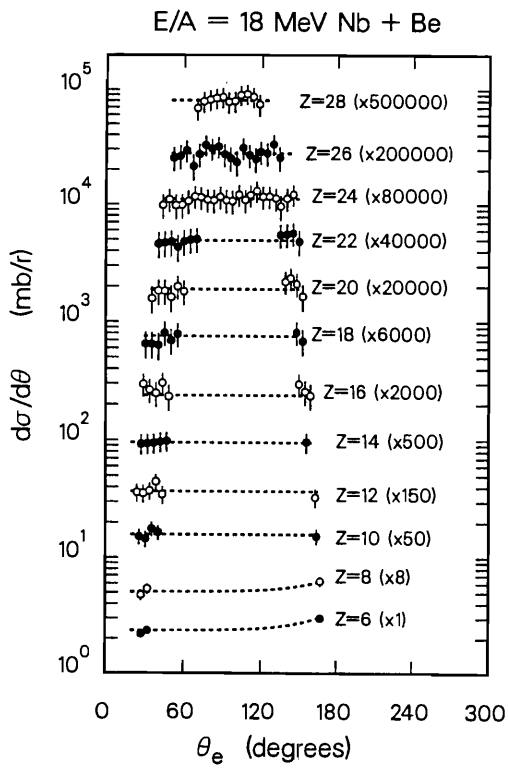

Fig. 8. Representative $d\sigma/d\theta$ angular distributions in the frame of the source system for the reaction $E/A = 18.0$ MeV Nb + Be. The dashed lines guide the eye.

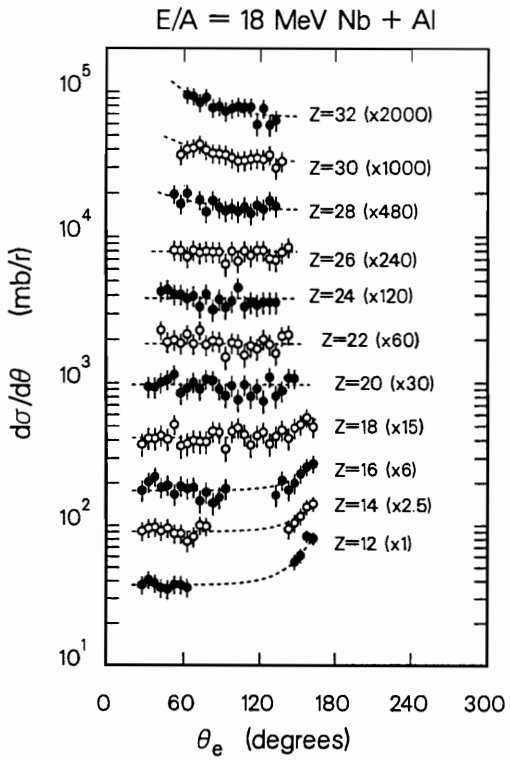

Fig. 9. Same as in fig. 8, for the reaction $E/A = 18.0$ MeV Nb + Al.

tions were not determined for large enough Z-values to see the projectile-like component. The distributions for the $E/A = 11.4$ MeV Nb + Al reaction in fig. 10, however, show the presence of this component. Here the onset of the forward peaking occurs at higher Z-values ($Z \geq 34$) than for the $E/A = 18.0$ MeV Nb + Al reaction. Here again one must consider the sequential evaporation of light particles from the primary fragments. At the higher bombarding energy, the excitation energy deposited in the primary fragments is presumably larger, and so the charge loss associated with sequential evaporation is greater. Hence, the projectile-like component extends down to lower Z-values. This may also explain why the projectile-like component was not seen for the reactions on the Be and C targets as the primary fragments would also be associated with lower excitation energies.

3.5. CROSS SECTIONS

Angle-integrated cross sections for the isotropic component were determined from the average $d\sigma/d\theta$ of the flat regions in the angular distributions. The shapes of the charge distributions for each of the reactions studied are shown in figs. 11-13.

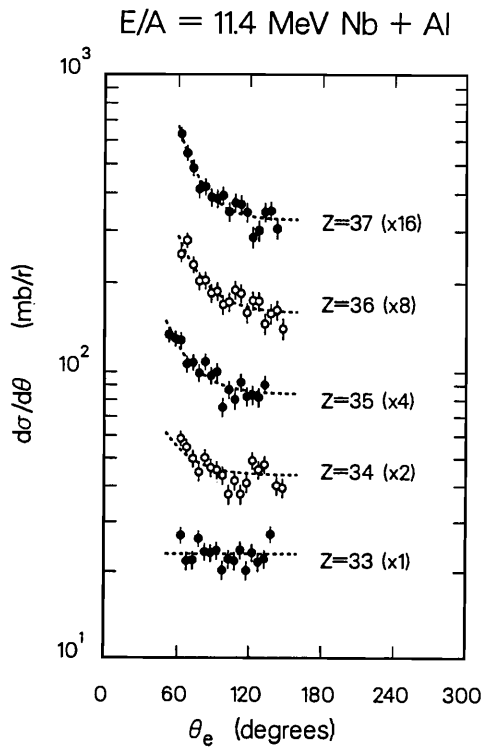

Fig. 10. Same as in fig. 9, for the reaction $E/A = 11.4$ MeV Nb + Al.

Also shown are charge distributions from ref. [8]) for bombarding energies of $E/A =$ 25.4 and 30.3 MeV, and from ref. [3]) for a bombarding energy of $E/A = 8.4$ MeV. The secondary Z-values corresponding to a primary symmetric division (sect. 3.6) are indicated by the arrows. The charge distributions are approximately symmetric about these arrows as is expected for binary decay.

The evolution of the shape of the charge distribution with increasing target mass can be understood [3]) in terms of the total mass of the system relative to the Businaro-Gallone point. For the Nb + Be system, the charge distribution is U-shaped indicating that it is slightly below the Businaro-Gallone point. For the Nb + C system, the charge distribution is flatter indicating that it is very near the Businaro-Gallone point. At the lowest bombarding energy, the heavier Nb + Al system shows a slight hint of a peak indicating that it is slightly above the Businaro-Gallone point.

For $Z < 20$, one notices some odd-even effects, especially for the lower bombarding energies. The yields for even Z-species typically are larger than the average trends and they are smaller for odd Z-species. While for $10 < Z < 20$, this structure is less noticeable at the higher bombarding energies, the structure for $Z \leq 10$ persists at all bombarding energies. For low excitation energies, shell and pairing effects associated with the saddle-point configuration, may give rise to fine structure in the

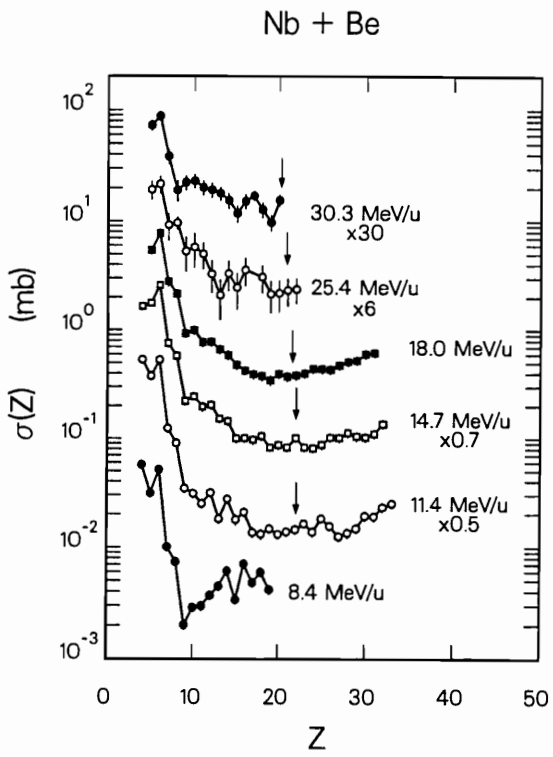

Fig. 11. Angle-integrated charge distributions of complex fragments associated with fusion-like reactions of Nb+Be at several bombarding energies. The arrows indicate the secondary Z-values at each bombarding energy associated with a primary symmetric division. Data from refs. [3,8]) have been included.

charge distributions. As the excitation energy increases, this fine structure should be progressively washed out due to sequential evaporation and be replaced by fine structure associated with the sequential evaporation itself. The structure observed at the higher bombarding energies is presumably related to the sequential evaporation. Since the structure for $10 < Z < 20$ washes out at the larger bombarding energies, it is more likely to be associated with shell and pairing effects at the saddle.

The excitation functions for fragments with $Z = 5$ and 10 and for the Z-species corresponding to symmetric division (see sect. 3.6) are shown in fig. 14. Data from refs. [3,8]) are also included in this figure. The sharp rise in all the excitation functions up to $E/A = 18.0$ MeV is reminiscent of the fission excitation functions at low bombarding energies. This is consistent with the rapid opening up of phase space for complex fragment decay. Above $E/A = 18.0$ MeV, the behavior of the excitation functions is quite different. The cross sections either are constant or decrease with bombarding energy. This difference in behavior may signal a change in the reaction mechanism, such as the evolution from complete fusion to incomplete fusion.

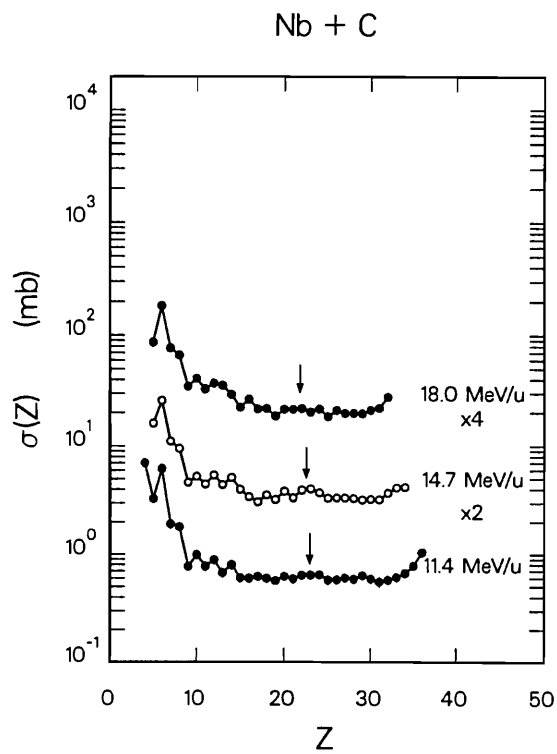

Fig. 12. Same as in fig. 11 for the Nb+C reactions.

3.6. COINCIDENCE DATA

The binary nature of the complex fragment events is most clearly seen in the coincidence data. Representative contour plots of the $Z_1 - Z_2$ correlation function are displayed in fig. 15. All the coincidence events lie in bands corresponding to an approximately constant value of $Z_1 + Z_2$. For comparison, the total charge of the reaction is indicated by the dashed lines in fig. 15. These bands do not extend out to the very asymmetric coincidences due to the symmetric placement of the detectors which favour the more symmetric coincidence events. The number of coincidence events associated with a fragment emitted forward in the source frame and backward in the source frame is plotted as a function of the fragment Z-value in fig. 16. For more asymmetric divisions, coincidences occur when the light fragment is emitted forward and the heavy fragment is emitted backward. This reduces any contributions to the coincidence yield from target-like and projectile-like fragments. The experimental placement of the detectors was not appropriate to record such coincidence events.

The difference between the average atomic charge associated with coincidence events $\langle Z_1 + Z_2 \rangle$ and the total atomic charge of the reaction $Z_p + Z_t$ reflects the charge lost by light-particle evaporation either before or after a major binary division. The

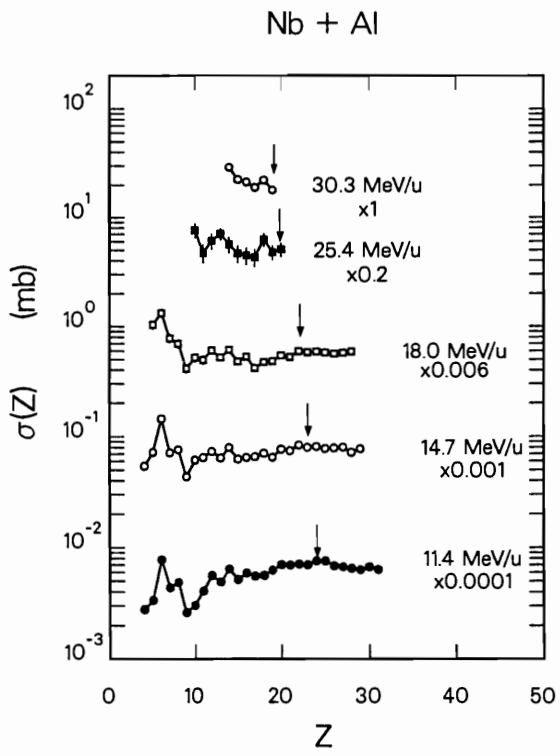

Fig. 13. Same as in fig. 11 for the Nb+Al reactions.

dependence of this missing charge $\Delta Z = Z_p + Z_t - \langle Z_1 + Z_2 \rangle$ on bombarding energy is displayed in fig. 17. In general, there is no dependence of ΔZ on the asymmetry of the binary division, except for a small dependence observed for the Nb+Al reaction at high bombarding energies. The values plotted in fig. 17 are for symmetric division ($Z_1 \approx Z_2$). The missing charge increases monotonically with both bombarding energy and target mass. Both increases reflect the increasing excitation energy of the CN, which results in larger light charged-particle multiplicities.

The secondary Z-value associated with the symmetric division of the CN is just $\frac{1}{2}\langle Z_1 + Z_2 \rangle$. Table 1 lists the values of such Z-values for all the reactions studied.

4. Statistical model calculations

4.1. THEORY

Complex fragment cross sections were calculated with the statistical model code GEMINI [47]). The code calculates the decay of compound nuclei by sequential binary decays. All possible binary divisions from light-particle emission to symmetric division are considered. The code employs a Monte Carlo technique to follow the

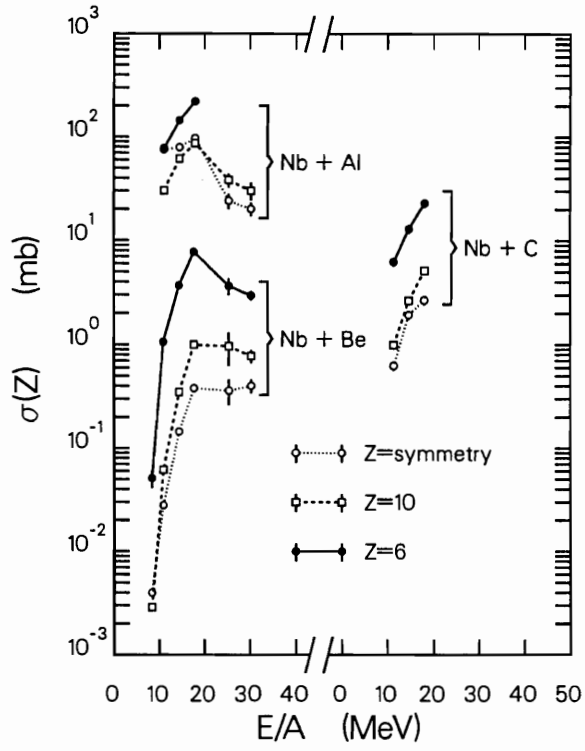

Fig. 14. Excitation functions for representative complex fragment species. The Z-value associated with symmetric division was obtained from the coincidence data. Date from refs. [3,8]) have been included.

decay chains of individual compound nuclei through sequential binary decays until the resulting products are unable to undergo further decay.

The decay width for the evaporation of fragments with $Z \leq 2$ is calculated using the Hauser-Feshbach formalism [48]). For the emission of a light particle (Z_1, A_1) of spin J_1 from a system (Z_0, A_0) of excitation energy E^* and spin J_0, leaving the residual system (Z_2, A_2) with spin J_2, the decay width is given by:

$$\Gamma_{J_2}(Z_1, A_1, Z_2, A_2) = \frac{2J_1+1}{2\pi\rho_0} \sum_{l=|J_0-J_2|}^{J_0+J_2} \int_0^{E^*-B-E_{\mathrm{rot}}(J_2)} T_l(\varepsilon)\rho_2(U_2, J_2)\,\mathrm{d}\varepsilon\,. \qquad (4)$$

In this equation l and ε are the orbital angular momentum and kinetic energy of the emitted particle, $\rho_2(U_2, J_2)$ is the level density of the residual system with thermal excitation energy

$$U_2 = E^* - B - E_{\mathrm{rot}}(J_2) - \varepsilon\,, \qquad (5)$$

B is the binding energy, $E_{\mathrm{rot}}(J_2)$ is the rotation plus deformation energy of the residual system, and ρ_0 is level density of the initial system.

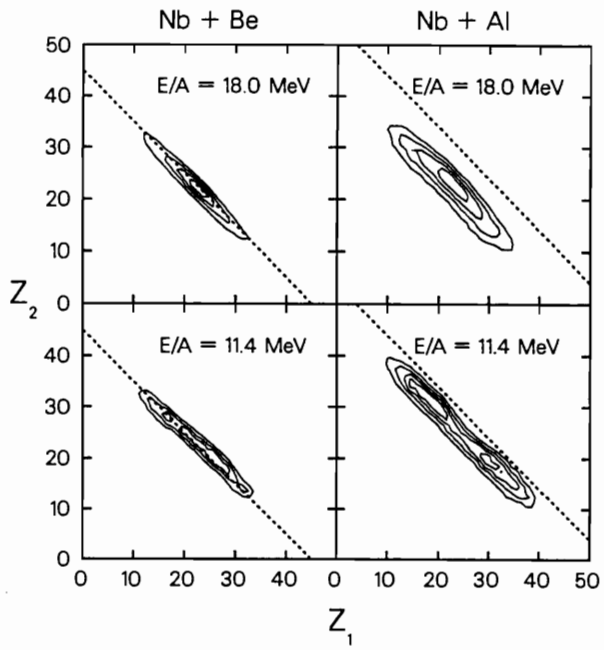

Fig. 15. Representative $Z_1 - Z_2$ contour plots for coincidence events. Z_1 and Z_2 refer to the Z-values of fragments detected in the two detectors.

The transmission coefficients $T_l(\varepsilon)$ were calculated with the sharp cut-off approximation for a classical system of absorptive radius R, and are given by:

$$T_l(\varepsilon) = \begin{cases} 0 & \text{for } \varepsilon < E_{\text{Coul}} + \dfrac{\hbar^2 l(l+1)}{2\mu R^2} \\ 1 & \text{for } \varepsilon \geq E_{\text{Coul}} + \dfrac{\hbar^2 l(l+1)}{2\mu R^2}, \end{cases} \tag{6}$$

where μ is the reduced mass. The Coulomb barriers E_{Coul} were calculated using the empirical expressions of Vaz and Alexander [49]) and the absorptive radius was taken as

$$\mathrm{R} = \begin{cases} 1.16\, A_2^{1/3} + 2.6 \text{ fm} & \text{for proton and neutron emission} \\ 1.16\, A_2^{1/3} + 3.7 \text{ fm} & \text{for alpha particle emission}. \end{cases} \tag{7}$$

In calculating the binding energy for heavy systems ($A > 12$), the masses of the initial and residual systems were obtained from the Yukawa-plus-exponential model of Krappe, Nix and Sierk [50]) without the shell and pairing correction terms. The parameters for this model were taken from the more recent fit to experimental masses of Möller and Nix [51]). These separation energies are expected to be more appropriate at high excitation energies where shell and pairing effects are predicted to wash out. For very light systems ($A \leq 12$), binding energies were calculated from

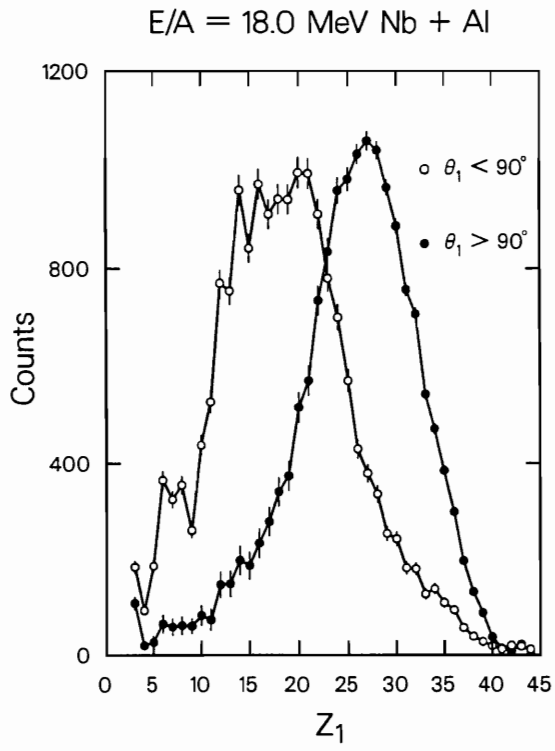

Fig. 16. Plot of the number of coincidence events as a function of the Z-value of one of the fragments. The two curves correspond to events where the fragment Z_1 was emitted at forward and backward angles by the source.

the experimental masses. The rotation plus deformation energy $E_{\rm rot}$ of a nucleus was taken from the RFRM calculations of Sierk [26]).

For binary divisions corresponding to the emission of heavier fragments, the decay width was calculated using the transition state formalism of Moretto [1]).

$$\Gamma(Z_1, A_1, Z_2, A_2) = \frac{1}{2\pi\rho_0} \int_0^{E^* - E_{\rm sad}(J_0)} \rho_{\rm sad}(U_{\rm sad}, J_0)\, {\rm d}\varepsilon\,, \tag{8}$$

where $U_{\rm sad}$ and $\rho_{\rm sad}$ are the thermal energy and level density of the conditional saddle-point configuration,

$$U_{\rm sad} = E^* - E_{\rm sad}(J_0) - \varepsilon\,, \tag{9}$$

$E_{\rm sad}(J_0)$ is the deformation plus rotation energy of the saddle-point configuration and ε now is the kinetic energy of the translational degree of freedom.

The deformation plus rotation energy was calculated with the RFRM using a two-spheroid parameterization for the shape of the conditional saddle-point configuration. This parameterization results in conditional barriers which are within

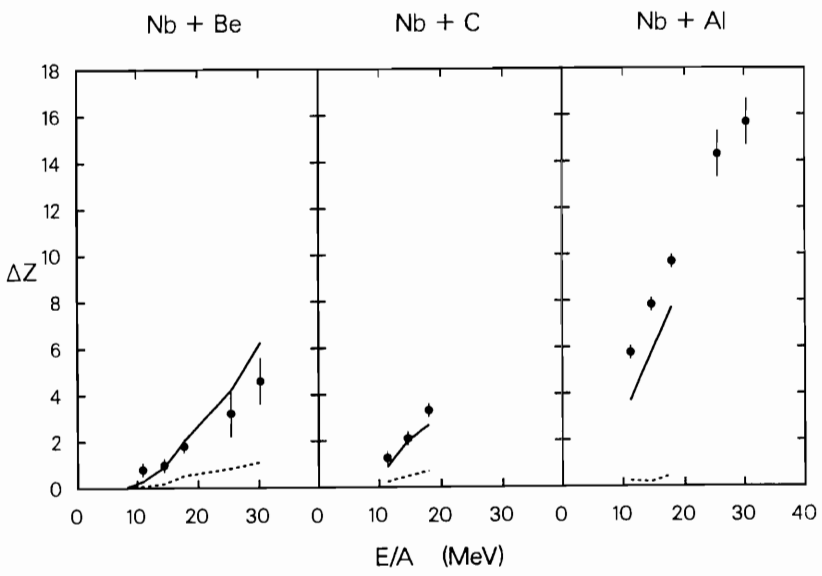

Fig. 17. Plot of the missing charge (ΔZ) determined from the coincidence data versus the bombarding energy. The missing charge is the difference between the total charge in the reaction ($Z_p + Z_t$) and the average sum of the Z-values of the coincidence fragments. For the Nb + Al reaction there is a small dependence of ΔZ on the asymmetry of the charge division. The data points plotted are for symmetric division. The dashed curve shows the predicted pre-scission charge loss due to light-particle emission from the CN (see text). The solid curve indicates the prediction of the total charge loss due to both pre-scission and post-scission light-particle emission (see sect. 4.4).

2 MeV of saddle-point energies calculated with more realistic shape parameterizations [52]) for $A_0 = 110$ [ref. [26])]. Better agreement is obtained for lighter nuclei. To correct for this difference to first order, the two-spheroid saddle-point energies were scaled by a constant factor for all mass asymmetries and angular momentum. The scaling factor was chosen so that for symmetric division, the scaled saddle-point energy was equal to the value calculated with the more realistic shape parameterization by Sierk [26,52]). For $Z_1 \leq 6$, these RFRM saddle-point energies [$E^{\mathrm{RFRM}}(J_0)$] were modified by

$$E_{\mathrm{sad}}(J_0) = E_{\mathrm{sad}}^{\mathrm{RFRM}}(J_0) - M_{\mathrm{Y+e}}(Z_1, A_1) + M_{\mathrm{exp}}(Z_1, A_1)\,, \tag{10}$$

where $M_{\mathrm{Y+e}}$ is the mass predicted by Yukawa-plus-exponential model without shell and pairing corrections and M_{exp} is the experimental mass. This modification is an attempt to introduce shell effects into the saddle-point energies for very asymmetric divisions, where one expects them to become more important.

For all level densities, the Fermi gas expression [53,54])

$$\rho(U, J) = (2J+1)\left[\frac{\hbar^2}{2\mathcal{I}}\right]^{3/2} \frac{\sqrt{a}}{12} \frac{\exp(2\sqrt{aU})}{U^2} \tag{11}$$

was used, where the $\mathcal{I}$ is the moment-of-inertia of the residual nucleus or saddle-point configuration. The level density parameter was taken as $a = A/8.5\ \mathrm{MeV}^{-1}$ for both the residual nucleus and in saddle point configurations.

The integrations in eqs. (4) and (8) were performed by first expanding the integrand around the lower limit, giving the approximate expression for the decay width for $Z_1 \leqslant 2$ as

$$\Gamma(Z_1, A_1, Z_2, A_2) = \frac{(2J_1+1)}{2\pi\rho_0} \sum_{J_2=0}^{\infty} \sum_{l=|J_0-J_2|}^{J_0+J_2} t_2 \rho_2(U_2, J_2)\,, \tag{12}$$

where now:

$$U_2 = E^* - B - E_{\mathrm{rot}}(J_2) - E_{\mathrm{Coul}} - \frac{\hbar^2 l(l+1)}{2\mu R^2}\,, \tag{13}$$

and the nuclear temperature is approximately:

$$t_2 = \sqrt{U_2/a}\,. \tag{14}$$

For $Z_1 > 2$

$$\Gamma(Z_1, A_1, Z_2, A_2) = \frac{1}{2\pi\rho_0} t_{\mathrm{sad}} \rho_{\mathrm{sad}}(U_{\mathrm{sad}}, J_0)\,, \tag{15}$$

where now:

$$U_{\mathrm{sad}} = E^* - E_{\mathrm{sad}}(J_0)\,, \tag{16}$$

and the temperature of the saddle-point configuration is approximately:

$$t_{\mathrm{sad}} = \sqrt{U_{\mathrm{sad}}/a}\,. \tag{17}$$

The secondary products formed in the binary decay of the initial system, (Z_1, A_1) and (Z_2, A_2) were allowed to undergo sequential binary decay. The spin of the residual system was chosen in a Monte Carlo fashion from the calculated partial decay widths $\Gamma_{J_2}(Z_1, A_1, Z_2, A_2)$. Its excitation energy was calculated as

$$E_2^* = U_2 - 2t_2 + E_{\mathrm{rot}}(J_2)\,. \tag{18}$$

For $Z_1 > 2$, the spin of the fragments was calculated in the sticking limit, i.e. for fragment 1

$$J_1 = (\mathcal{I}_1/\mathcal{I})J_0\,, \tag{19}$$

where $\mathcal{I}_1$ is the moment of inertia of the fragment and $\mathcal{I}$ is the total moment of inertia of the system. Its excitation energy was derived assuming equal temperatures for the two fragments, as

$$E_1^* = \frac{A_1}{A_0}[U_{\mathrm{sad}} - \mathrm{t_{sad}}] + E_{\mathrm{rot}}(J_1)\,. \tag{20}$$

This is strictly valid only when the saddle- and scission-point configurations are degenerate and this is approximately true for the systems of this work. However, eq. (20) *is not applicable for heavier systems.*

4.2. CROSS SECTIONS

Cross sections were calculated for all Z-species with the code GEMINI. As input for these calculations, the initial population of compound nuclei was assumed to arise from complete fusion reactions. The excitation energy of the compound nuclei was derived from a Q-value for fusion calculated using the experimental masses for the target and projectile nuclei and the Yukawa-plus-exponential model mass without shell and pairing corrections for the compound system. Similar assumptions have been used by a number of authors in the calculation of fission excitation functions [14,19,20,23,24]). The rationale for this assumption is that at the high excitation energies and angular momentum induced in the reactions of this work, shell and pairing effects are expected to be washed out.

The compound-nucleus spin distribution was assumed to be given by the sharp-cut-off approximation with the maximum spin (J_{max}) being left as a fitting parameter. The value of J_{max} was adjusted so as to give the best fit to the experimental cross sections. The model can be tested by checking whether it is possible to reproduce both the shape and magnitude of the experimental charge distribution with a reasonable value of J_{max}. The value of J_{max} must be less than the critical angular momentum at which the symmetric barrier vanishes (J_{crit}) or else the reaction is expected to proceed through the fast-fission mechanism. The symmetric barrier is the first conditional barrier to vanish as the angular momentum is increased. For the compound systems of this work, the values of J_{crit} predicted by the RFRM are $\approx 78\hbar$ [ref. [26])].

Charge distributions calculated with the code GEMINI are compared to the experimental data in figs. 18–20. The values of the excitation energy and maximum spin employed in the calculations are indicated in the figures. For the Nb + Be and C reactions, it was possible to reproduce both the shape and magnitude of the experimental charge distributions using a value of J_{max} less than J_{crit}. For high Z-values, the calculated charge distributions shows the presence of a large evaporation residue peak. This peak is associated almost entirely with "classical evaporation residues"; which result from systems which decay only via the evaporation of $Z \leq 2$ particles. The cross sections for the "classical evaporation residues" are indicated by the dashed curves in figs. 18–20. The evaporation of light particles is predicted to be the dominant decay mode. For example, in the $E/A = 18.0$ MeV Nb + C reactions, "classical evaporation residues" represent 80% of the initial fusion cross section. The emission of one complex fragment with $Z > 2$ is relatively rare and the emission of more than one complex fragment is negligible (a probability of $\approx 0.4\%$ in the above reaction).

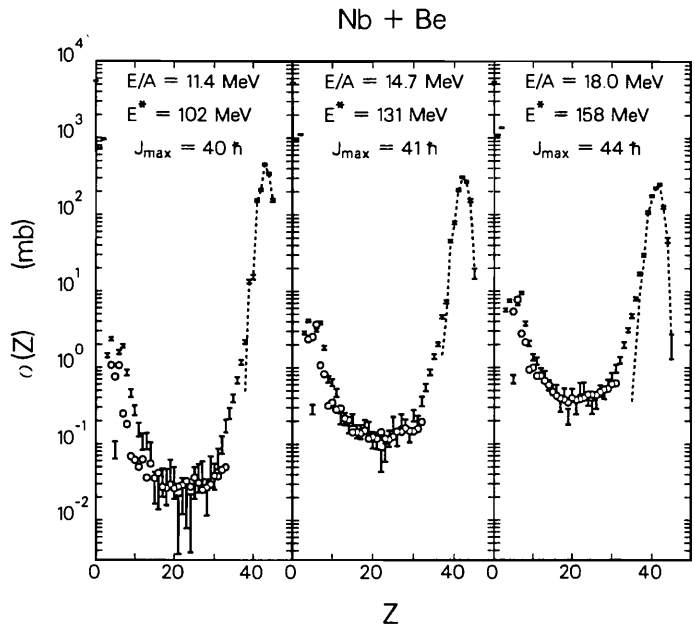

Fig. 18. Comparison of experimental and calculated charge distributions for the Nb+Be reaction. The experimental data are indicated by the hollow circles and the calculated values are shown by the error bars. The dashed curve indicates the cross sections associated with classical evaporation residues which decay only by the emission of light particles ($Z \leq 2$).

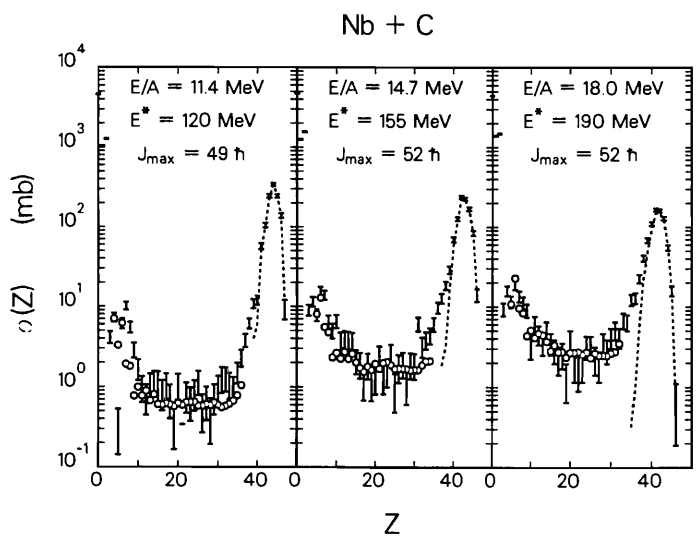

Fig. 19. Same as in fig. 18, for the Nb+C reactions.

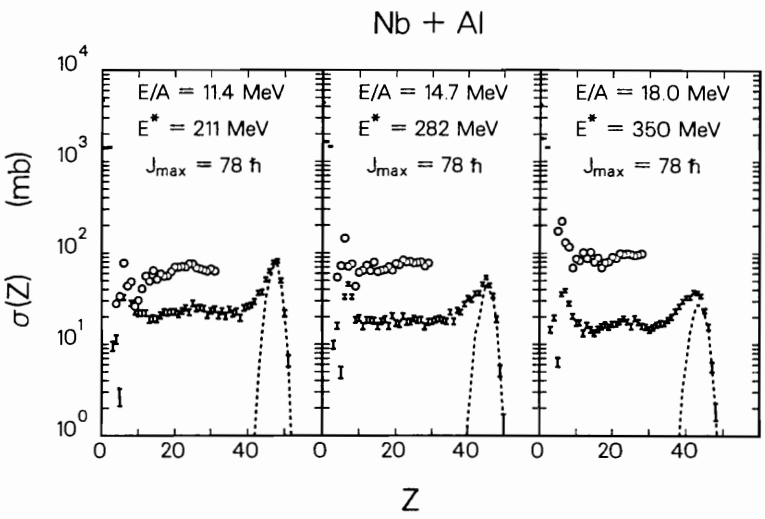

Fig. 20. Same as in fig. 18, for the Nb+Al reactions.

In the Nb+Al reaction, one finds quite a different picture. It was found possible to reproduce the shape but not magnitude of the experimental data with $J_{max} < J_{crit}$. The calculations shown in fig. 20 were obtained with $J_{max} = J_{crit}$ and significantly underestimate the experimental data. Even if one were to change the relative strengths of the light particle and complex fragment decay channels, it would be impossible to obtain cross sections as large as those determined experimentally. This implies that most of the complex fragments are being produced in reactions with L-waves of angular momentum greater than J_{crit}. This may indicate that for the Nb+Al reaction fast-fission is the dominant production mechanism for complex fragment production. In contrast, for $E/A > 20$ MeV, the Nb+Al source velocities are consistent with a mixture of complete and incomplete fusion [8]). Furthermore, all of the complex fragment yield can be accounted for by a mixture of complete and incomplete fusion with the dominant portion associated with the latter process. Because of the incomplete transfer of angular momentum, the maximum spin of the CN formed in incomplete fusion reactions is less than J_{crit}. Thus, at the higher bombarding energies emission of complex fragments from CN (formed in incomplete fusion reactions) is still important.

Calculations were also performed for the higher and lower bombarding energy data for the Nb+Be reactions of refs. [3,8]). The calculated charge distributions are compared to the experimental data in figs. 21 and 22. For the $E/A = 25.4$ and 30.3 MeV reactions, good reproductions of the shape and magnitude of the experimental charge distribution were again obtained by adjusting the value of J_{max}. Even at these bombarding energies, complex fragment emission is still a relatively rare process compared to light particle evaporation. Even for the $E/A = 8.4$ MeV data

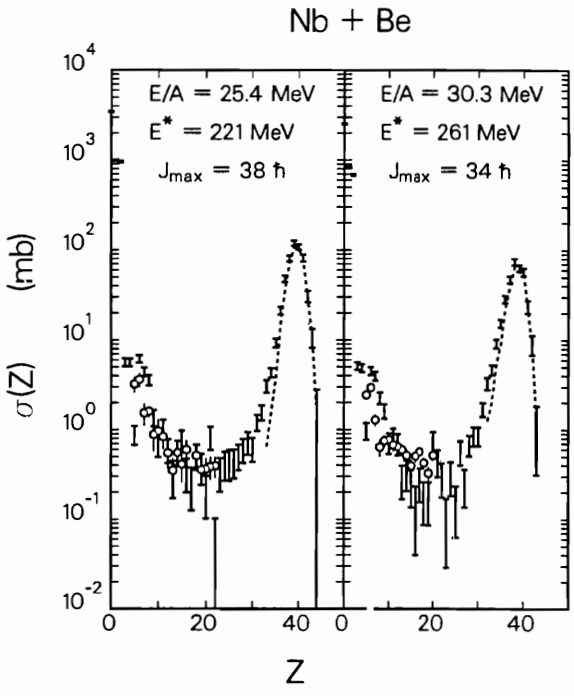

Fig. 21. Same as in fig. 18, for the Nb+Be reactions of ref. [8]).

of fig. 22, the calculations reproduce the general shape of the experimental data but miss some of the specific features. For example, the experimental cross sections increase for $Z > 9$ in disagreement with the calculations. As suggested previously, this may be due to shell effects which should become more important at the lower excitation energies and were not included in the calculations.

Although complex fragment emission is rare in the Nb+Be and C reactions, it is associated almost entirely with the highest partial waves. Fig. 23 illustrates the dependence of the predicted complex fragment cross sections on J_{max}. Small changes in J_{max} produce large changes in both the shape and magnitude of the charge distributions. This underlies the importance of being able to simultaneously reproduce both the shape and magnitude of the experimental charge distributions and gives one confidence in the validity of the model.

4.3. EXTRACTED J_{max} VALUES

In order to determine the significance of the previous calculations, one must consider whether the values J_{max} used to fit the data are reasonable. These values are plotted as a function of bombarding energy in figs. 24 and 25. The error bars shown in these figures give an indication of the systematic error associated with the

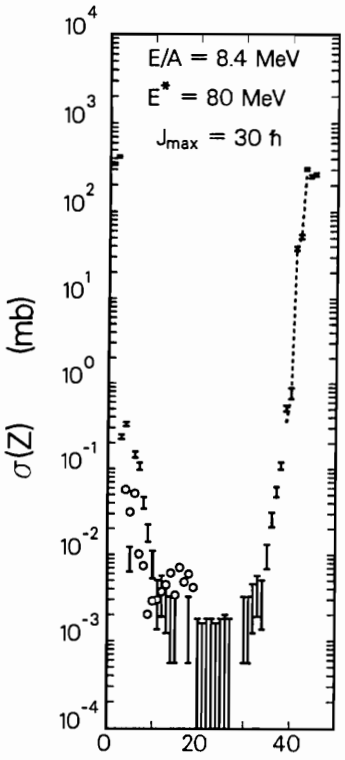

Fig. 22. Same as in fig. 18, for the Nb + Be reaction of ref. [3]).

calculations. In determining these errors, one should note that the values of most of the parameters needed in the statistical model calculations are uncertain. Small changes in many of these parameters will result in large changes in the predicted complex fragment cross sections. Also, the use of more realistic CN spin distributions than the sharp-cut-off approximation are expected to enhance the predicted complex fragment cross sections [24]). The error bars were obtained by assuming that these effects result in an uncertainty of 300% in the calculated cross sections. This is not a particularly extreme assumption. However, because of the strong dependence of the calculated cross sections on J_{max}, these error bars are not very large.

Between $E/A = 10$ and 20 MeV, the extracted values of J_{max} show very little dependence on bombarding energy for both the Nb + Be and C reactions. For the higher bombarding energies in the Nb + Be reactions, the extracted J_{max} values actually decrease with bombarding energies.

The extracted values are compared to the predictions of the Bass model [55]) and the extra-push model [56,57]) in figs. 24 and 25. In the high bombarding energy regime, the limiting angular momentum for fusion in the Bass model is given by

$$L_{max} = L_1/f, \tag{21}$$

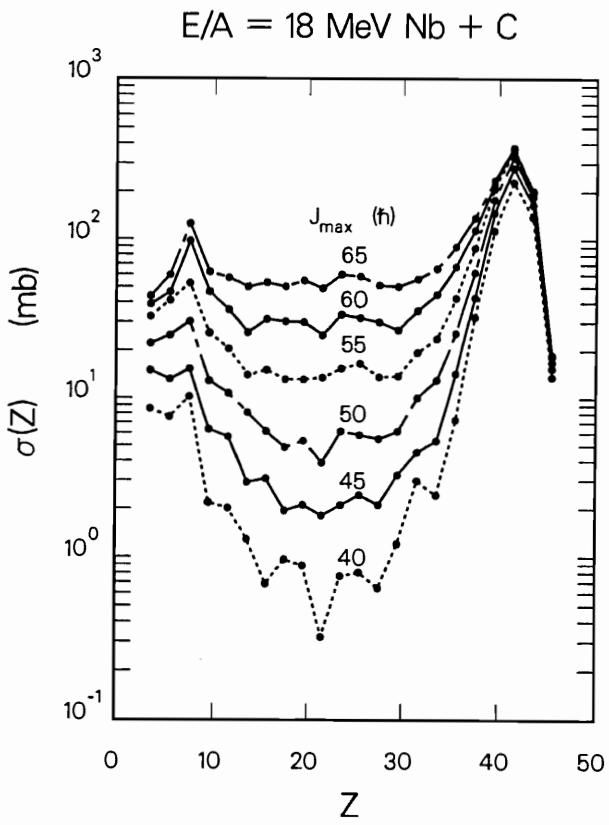

Fig. 23. Representative plot showing the dependence of the predicted charge distributions on the maximum angular momentum for fusion (J_{max}).

where L_1 is the angular momentum at which the effective two-body potential between touching projectile and target nuclei becomes repulsive, and f is the fraction by which the orbital angular momentum is reduced by frictional forces after contact. The curves in figs. 24 and 25 were derived using values of L_1 calculated with the 1977 Bass potential [58]) and assuming $f = \frac{5}{7}$ (rolling limit). The parameters used in the extra-push model are those obtained by fitting fusion excitation functions for Pb-induced reactions [57]).

The extracted values of J_{max} are in good agreement with these predictions. However, the lowering of J_{max} at the high bombarding energies is not reproduced by the models. Whether this effect is real is difficult to ascertain at present. Such an effect may be produced by mechanisms which decrease the binary decay probability such as the pre-equilibrium emission of nucleons from the CN or a transient binary decay rate [30-33]).

Except for some possible problems for $E/A > 20$ MeV, the Nb + Be and C experimental charge distributions can be reproduced with statistical model calculations

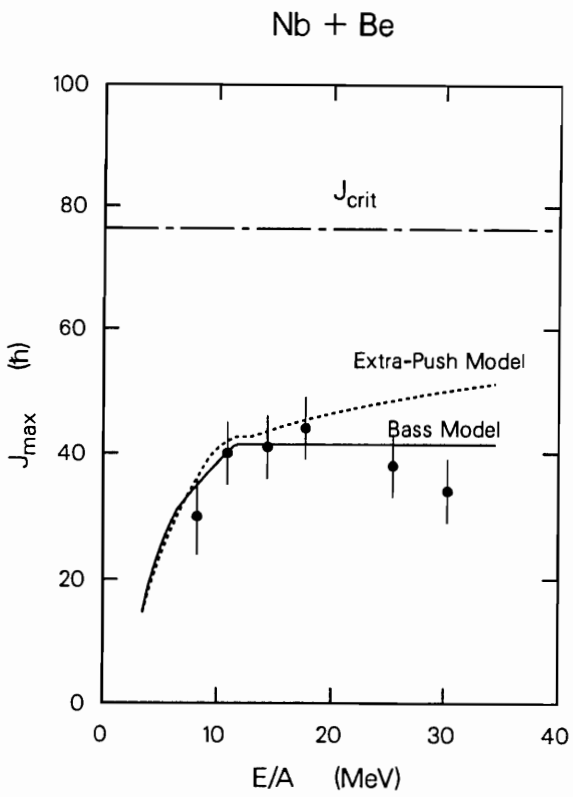

Fig. 24. Plot showing the maximum angular momentum for fusion (J_{max}) obtained by fitting the experimental charge distributions as a function of bombarding energy for the Nb + Be reactions. The dashed and solid curve show the predictions of the extra-push and Bass models, respectively. The chain dashed lines indicated the angular momentum where the barrier for symmetric division vanishes.

employing RFRM conditional barriers and with CN spin distributions consistent with fusion models.

The predictions of the extra-push and Bass models for the Nb + Al reactions are displayed in fig. 26. For the bombarding energies of interest, the predicted values of J_{max} are greater than J_{crit}, the angular momentum at which the symmetric conditional barrier vanishes. This is in accord with the statistical model analysis of the experimental charge distributions (sect. 4.2). Therefore, these fusion models are useful for determining the maximum L-waves for which fusion and/or fast-fission processes occurs. Higher L-waves may be associated with incomplete fusion and deep inelastic interactions.

4.4. MISSING CHARGE

The missing charge ΔZ associated with complex fragment events was obtained from the statistical model calculations. It includes the charge due to light-particle

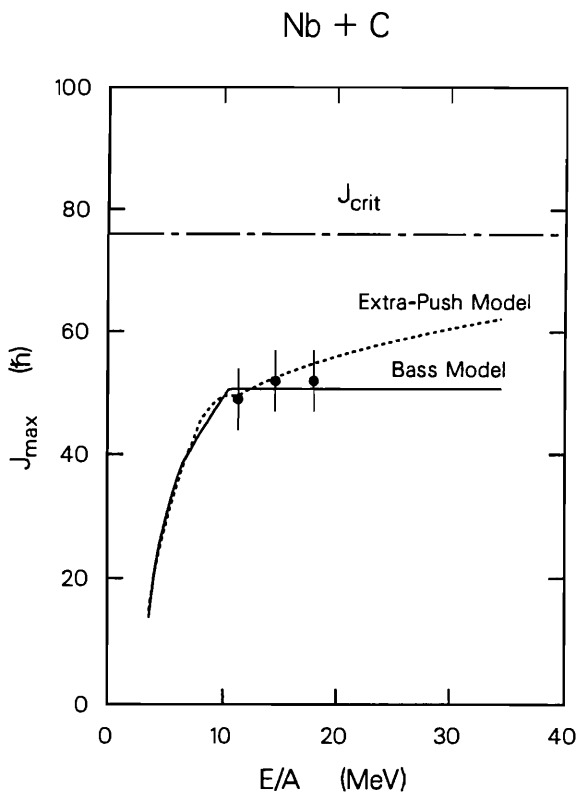

Fig. 25. Same as in fig. 24, for the Nb+C reactions.

evaporation from both the CN prior to scission, and from the primary fragments after scission. The calculated pre-scission and total missing charge is compared to the experimental data in fig. 17. The calculated missing charge is in excellent agreement with experiment, which again supports the validity of the statistical model calculations. The majority of the charge loss is predicted to be post-scission. For the Nb+Be and C reactions, the small pre-scission component is a consequence of the large sensitivity of the complex fragment decay width on angular momentum and excitation energy. If the CN evaporates a light particle and consequently reduces its angular momentum and excitation energy, the complex fragment decay width drops significantly. Therefore if complex fragment emission occurs at all, it occurs early in the decay chain.

Recently it has been proposed, that due to nuclear dissipation, the decay rate for fission and presumably other binary decay modes takes a finite time to build up to its final value [29-33]). During this time, light-particle evaporation is unhindered. Such an effect would increase the pre-scission light-particle evaporation at the expense of the post-scission evaporation. Similarly pre-equilibrium emission of nucleons would also alter the ratios of pre- to post-scission evaporation. These effects cannot

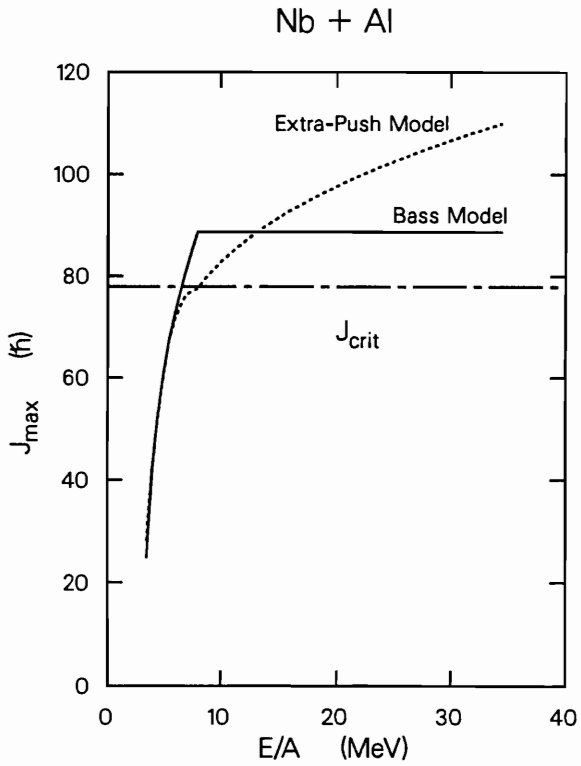

Fig. 26. Same as in fig. 24 for the Nb+Al reactions.

be large for the Nb+Be and C reactions at $E/A < 20$ MeV, as they would greatly reduce the probability of complex fragment emission.

5. Conclusions

Complex fragments with $3 < Z \leqslant 35$ have been detected in Nb+Be, C, and Al reactions. Velocity spectra and angular distributions indicate the presence of three components: a target-like component corresponding to low Z-values emitted at backward angles; a projectile-like component associated with fragments of high Z-values emitted at forward angles; and an isotropic component ($d\sigma/d\theta = \text{const.}$) for all Z-values. For the Nb+Be and C reactions, the isotropic component has been shown to result from the binary decay of CN formed in a complete fusion reaction. The associated charge distributions can be reproduced by statistical model calculations employing rotating finite-range model conditional barriers and fusion cross sections predicted by the Bass and extra-push models. This work confirms the importance of the finite-range effect for very light nuclei.

For the Nb+Al reactions at the present bombarding energies, the isotropic component, in addition to contributions from CN decay from complete fusion,

requires an additional component which may be associated with the fast-fission mechanism.

The authors wish to thank GSI for its kind hospitality and in particular the crew of the UNILAC for supplying the excellent Nb beams. The authors also wish to thank A. Sierk for supplying his program to calculate RFRM conditional barriers. This work was supported by the Director, Office of Energy Research, Division of Nuclear Physics of the Office of High Energy and Nuclear Physics of the US Department of Energy under Contracts DE-AC03-76SF00098 and DE-ASO2-76ER04052.

References

1) L.G. Moretto, Nucl. Phys. **A247** (1975) 211
2) L.G. Sobotka, M.L. Padgett, G.J. Wozniak, G. Guarino, A.J. Pacheco, L.G. Moretto, Y. Chan, R.G. Stokstad, I. Tserruya and S. Wald, Phys. Rev. Lett. **51** (1983) 2187
3) L.G. Sobotka, M.A. McMahan, R.J. McDonald, C. Signarbieux, G.J. Wozniak, M.L. Padgett, J.H. Gu, Z.H. Liu, Z.Q. Yao and L.G. Moretto, Phys. Rev. Lett. **53** (1984) 2004
4) M.A. McMahan, L.G. Moretto, M.L. Padgett, G.J. Wozniak, L.G. Sobotka and M.G. Mustafa, Phys. Rev. Lett. **54** (1985) 1995
5) D. Jacquet, E. Duek, J.M. Alexander, B. Borderie, J. Galin, D. Gardes, D. Guerreau, M. Lefort, F. Monnet, M.F. Rivet and X. Tarrago, Phys. Rev. Lett. **53** (1984) 2226
6) M. Conjeaud, S. Harar, M. Mostefai, E.C. Pollacco, C. Volant, Y. Cassagnou, R. Dayras, R. Legrain, H. Oeschler and Saint-Laurent, Phys. Lett. **B159** (1985) 244
7) G. Auger, D. Jouan, E. Plagnol, F. Pougheon, F. Naulin, H. Doubre and C. Grégoire, Z. Phys. **A321** (1985) 243
8) R.J. Charity, D.R. Bowman, Z.H. Liu, R.J. McDonald, M.A. McMahan, G.J. Wozniak, L.G. Moretto, S. Bradley, W.L. Kehoe and A.C. Mignerey, Nucl. Phys. **A476** (1988) 516
9) F. Auger, B. Berthier, A. Cunsolo, A. Foti, W. Mittig, J.M. Pascaud, E. Plagnol, J. Québert and J.P. Wieleczko, Phys. Rev. **C35** (1987) 190
10) D.R. Bowman, W.L. Kehoe, R.J. Charity, M.A. McMahan, A. Moroni, A. Bracco, S. Bradley, I. Iori, R.J. McDonald, A.C. Mignerey, L.G. Moretto, M.N. Namboodiri and G.J. Wozniak, Phys. Lett. **B189** (1987) 282
11) M. Beckerman and M. Blann, Phys. Rev. **C17** (1978) 1615
12) F. Plasil, R.L. Ferguson, R.L. Hahn, F.E. Obenshain, F. Pleasonton and G.R. Young, Phys. Rev. Lett. **45** (1980) 330
13) C. Cabot, H. Gauvin, Y. LeBeyec, H. Delagrange, J.P. Dufour, A. Fleury, Y. Llabador and J.M. Alexander, J. de Phys. Coll. **41** (1980) C10-234
14) D.J. Hinde, J.R. Leigh, J.O. Newton, W. Galster and S.H. Sie, Nucl. Phys. **A385** (1982) 109
15) M. Blann and T.T. Komoto, Phys. Rev. **C26** (1982) 472
16) B. Sikora, W. Scobel, M. Beckerman, J. Bisplinghoff and M. Blann, Phys. Rev. **C25** (1982) 1446
17) G. Guillaume, J.P. Coffin, F. Rami, P. Engelstein, B. Heusch, P. Wagner, P. Fintz, J. Barrette and H.E. Wegner, Phys. Rev. **C26** (1982) 2458
18) S.E. Vigdor, H.J. Karwowski, W.W. Jacobs, S. Kailas, P.P. Singh, F. Soga and T.G. Throne, Phys. Rev. **C26** (1982) 1035
19) D.J. Hinde, J.O. Newton, J.R. Leigh, and R.J. Charity, Nucl. Phys. **A398** (1983) 308
20) J. van der Plicht, H.C. Britt, M.M. Fowler, Z. Fraenkel, A. Gavron, J.B. Wilhelmy, F. Plasil, T.C. Awes and G.R. Young, Phys. Rev. **C28** (1983) 2022
21) F. Plasil, T.C. Awes, B. Cheynis, D. Drain, R.L. Ferguson, F.E. Obenshain, A.J. Sierk, S.G. Steadman and G.R. Young, Phys. Rev. **C29** (1984) 1145

22) K.T. Lesko, W. Henning, K.E. Rehm, G. Rosner, J.P. Schiffer, G.S.F. Stephans, B. Zeidman and W.S. Freeman, Phys. Rev. Lett. **55** (1985) 803
23) A. Gavron, J. Boissevain, H.C. Britt, K. Eskola, P. Eskola, M.M. Fowler, H. Ohm. J.B. Wilhelmy, T.C. Awes, R.L. Ferguson, F.E. Obenshain, F. Plasil, G.R. Young and S. Wald, Phys. Rev. **C30** (1984) 1550
24) R.J. Charity, J.R. Leigh, J.J.M. Bokhorst, A. Chatterjee, G.S. Foote, D.J. Hinde, J.O. Newton, S. Ogaza and D. Ward, Nucl. Phys. **A457** (1986) 441
25) S. Cohen, F. Plasil and W.J. Swiatecki, Ann. of Phys. **82** (1974) 557
26) A.J. Sierk, Phys. Rev. **C33** (1986) 2039
27) A.J. Sierk, Phys. Rev. Lett. **55** (1985) 582
28) U.L. Businaro and S. Gallone, Nuovo Cim. **1** (1955) 629, 1277
29) H.A. Kramers, Physica **7** (1940) 284
30) P. Grangé and H.A. Weidenmüller, Phys. Lett. **B96** (1980) 26
31) P. Grangé, J.Q. Li and H.A. Weidenmüller, Phys. Rev. **C27** (1983) 2063
32) H.A. Weidenmüller and J.S. Zhang, Phys. Rev. **C29** (1984) 879
33) S. Hassani and P. Grangé, Phys. Lett. **B137** (1984) 281
34) R.W. Hasse and W. Stoker, Phys. Lett. **B44** (1973) 26
35) G. Sauer, H. Chandra and U. Mosel, Nucl. Phys. **A264** (1976) 221
36) M. Diebel, K. Albrecht and R.W. Hasse, Nucl. Phys. **A355** (1981) 66
37) X. Campi and S. Stringari, Z. Phys. **A309** (1983) 239
38) D. Dalili, J. Németh and C. Ngô, Z. Phys. **A321** (1985) 335
39) D.J. Fields, W.G. Lynch, T.K. Nayak, M.B. Tsang, C.B. Chitwood, C.K. Gelbke, R. Morse, J. Wilczynski, T.C. Awes, R.L. Ferguson, F. Plasil, F.E. Ovenshain and G.R. Young, Phys. Rev. **C34** (1986) 536
40) M. Fatyga, K. Kwiatkowski, V.E. Viola, W.G. Wilson, M.B. Tsang, J. Pochodzalla, W.G. Lynch, C.K. Gelbke, D.J. Fields, C.B. Chitwood, Z. Chen and T. Nayak, Phys. Rev. Lett. **58** (1987) 2527
41) K. Kwiatkowski, J. Bashkin, H. Karwowski, M. Fatyga and V.E. Viola, Phys. Lett. **B171** (1986) 41
42) M. Fatyga, R.C. Byrd, K. Kwiatkowski, W.G. Wilson, L.W. Woo, V.E. Viola, H.J. Karwowski, J. Jastrzebski and W. Skulski, Phys. Lett. **B185** (1987) 321
43) V.E. Viola, B.B. Back, K.L. Wolf, T.C. Awes, C.K. Gelbke and H. Breuer, Phys. Rev. **C26** (1982) 178
44) V.E. Viola, K. Kwiatkowski and M. Walker, Phys. Rev. **C31** (1985) 1550
45) L.G. Moretto, S.K. Kataria, R.C. Jared, R. Schmitt and S.G. Thompson, Nucl. Phys. **A255** (1975) 491
46) R. Babinet, L.G. Moretto, J. Galin, R. Jared, J. Moulton and S.G. Thompson, Nucl. Phys. **A258** (1976) 172
47) R.J. Charity, private communication
48) H. Hauser and H. Feshbach, Phys. Rev. **87** (1952) 366
49) L. Vaz and J.M. Alexander, Z. Phys. **A318** (1984) 231
50) H.J. Krappe, J.R. Nix and A.J. Sierk, Phys. Rev. **C20** (1979) 992
51) P. Möller and J.R. Nix, Nucl. Phys. **A361** (1981) 117
52) K.T. Davies and A.J. Sierk, Phys. Rev. **C31** (1985) 915
53) H.A. Bethe, Phys. Rev. **50** (1936) 332
54) A. Bohr and B. Mottelson, Nuclear structure, vol. 1 (Benjamin, New York, 1969)
55) R. Bass, Nucl. Phys. **A231** (1974) 45
56) W.J. Swiatecki, Nucl. Phys. **A376** (1982) 275
57) S. Bjørnholm, W.J. Swiatecki, Nucl. Phys. **A391** (1982) 471
58) R. Bass, Phys. Rev. Lett. **39** (1977) 265